

Surface roughness effect on dynamic wettability in imbibition process

Guang Yang, Moran Wang^{*}

Department of Engineering Mechanics, Tsinghua University, Beijing 100084, China

ARTICLE INFO

Keywords:

Dynamic contact angle
Micro-channel flow
Multiphase LBM
Random roughness

ABSTRACT

Dynamic wetting on rough surface is important in imbibition processes in micro- and nano- channels. Due to high computational costs, the previous studies by direct numerical simulations mostly adopted two-dimensional (2D) simplifications of surface with roughness. The cutting-edge advances in high performance computing make it possible to conduct three-dimensional (3D) direct simulations. This work presents 3D simulations on channel flows with roughness on walls via the GPU-based multiphase lattice Boltzmann method (LBM). The effects from 3D roughness morphology are investigated. In contrast to the wettability alternation in 2D rough ones, the 3D rough hydrophilic surfaces remain hydrophilic and Wenzel state at even low capillary numbers (Ca). The apparent contact angle follows the hydrodynamic model on rough surfaces except for a more sensitivity to Ca . The results also indicate that the 2D simplifications overestimate the pressure drop for rough channels, while underestimate over 20% for smooth channels. Therefore, it is crucial to consider 3D structures of surface roughness for dynamic wetting in real channels.

1. Introduction

Imbibition process, also known as capillary rise, plays an important role at micro and nano-scale, such as industrial applications involving porous media [1,2] like petroleum engineering [3], carbon capture storage [4], “lab on chip” [5] and related microfluidic and nanofluidic devices [6,7]. Due to the dynamic nature, the dynamic wetting effect is not negligible in predictions of the interface position, in other words, the flow rate via the famous Washburn model [7–11]. Theoretically, the motion of the three-phase contact line, which governs the dynamic wetting effect, is contradictory to the conventional Navier-Stokes non-slip boundary condition [12]. Therefore, several theoretical models have been proposed including hydrodynamic model [13,14], molecular-kinetic model [15], hybrid model [16] and diffuse-interface model [17] to explain the mechanism of the contact line motion on smooth surfaces.

Apart from the theoretical models, numerical simulations have been also conducted. Some researchers employed macroscopic methods, such as volume of fluid [18,19] and level-set methods [20], to study the dynamic contact angle. Since additional experimental correlations and theoretical models were required, the accuracy of those models depended on the models and correlations incorporated rather than the physics at the three-phase contact line region. Thus, macroscopic methods are not suitable for mechanism studies. On the other hand, microscopic

molecular dynamics (MD) as well as hybrid methods have been reported studying dynamic wetting [21–24]. Although microscopic simulations can provide more details in physics, the computational domain is limited due to high computational costs.

Therefore, it is natural to consider mesoscopic methods, among which the lattice Boltzmann method (LBM) is widely known for its solid physical foundation, easy extensions to new models and schemes, and high computing efficiency [25–27]. Since LBM employs the diffuse interface model, the slip model and the dynamic contact angle can be achieved spontaneously [17,28,29]. Latva-Kokko and Rothman [28] analyzed the slip length and scaling of the dynamic contact angle in LBM via the hydrodynamic model [14]. Nevertheless, their results were of lattice unit, which was hard to apply to the real-world units.

However, real surfaces are not ideally smooth. The effect of surface roughness has been widely studied in numerous transport phenomena, including single-phase flow in micro-devices [30] and porous media [31], multiphase flows [32] and electro-kinetics [33,34]. As for wetting phenomena, though the Wenzel model [35] and Cassie-Baxter model [36] provide quantitatively relationships between the apparent contact angle θ_a and the intrinsic contact angle θ_i on the rough surface, such results are not applicable to the dynamic situations due to the non-equilibrium states [37–39]. Recently, roughness effect on the dynamic wetting has attracted more and more attention. Many researchers studied roughness induced hydrophobicity to reduce drag force [40,41].

^{*} Corresponding author.

E-mail address: mrwang@tsinghua.edu.cn (M. Wang).

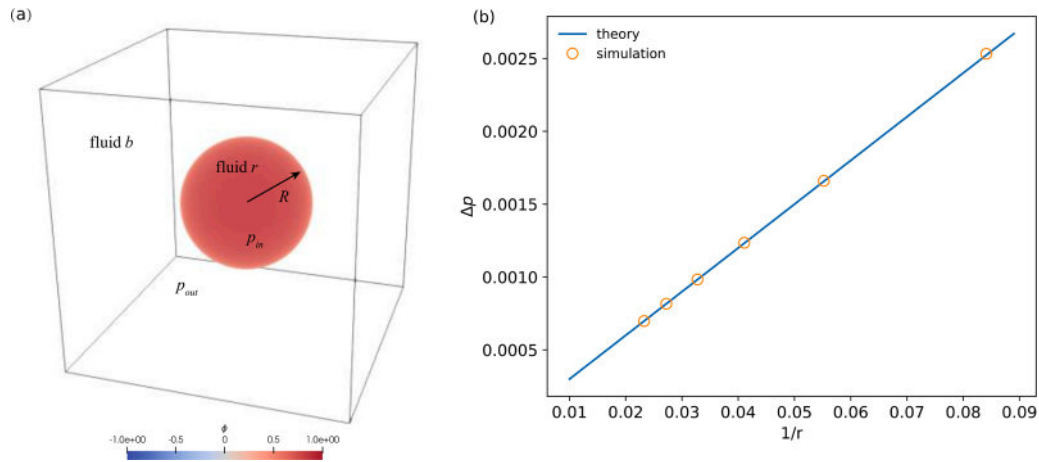


Fig. 1. (a) Illustration of the stationary droplet benchmark. Initially a cubic bubble is placed at the center of the domain. Due to surface tension, the bubble will deform to sphere. (b) The pressure difference inside and outside the bubble, compared with the theory. Here, the theory denotes the Young-Laplace equation, i.e., Eq. (16).

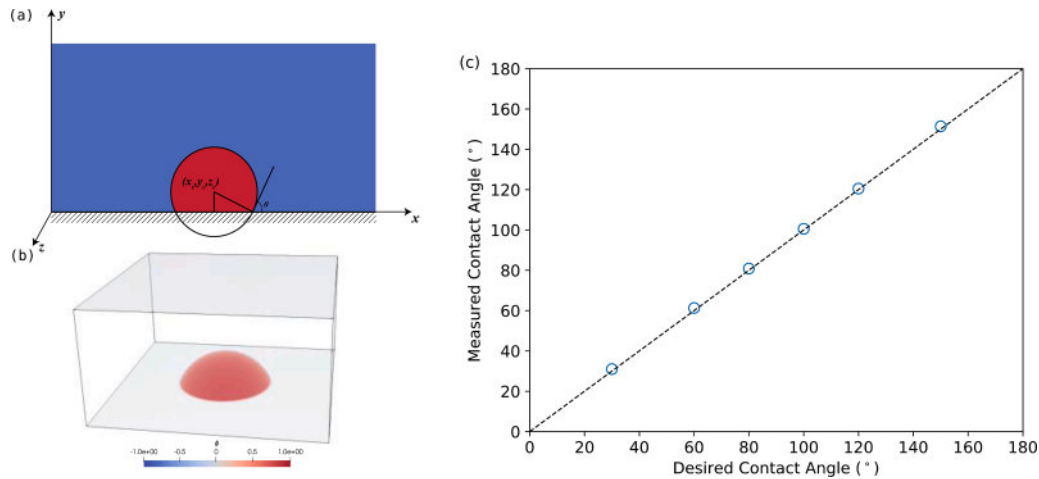


Fig. 2. (a) Illustration of the contact angle. A sphere is fitted with all the interfacial points. Based on the radius and center of the sphere, contact angle is derived via Eq. (17). (b) Illustration of a simulated droplet with the contact angle $\theta = 30^\circ$. (c) Comparison between the desired contact angles and the measured contact angles in simulations.

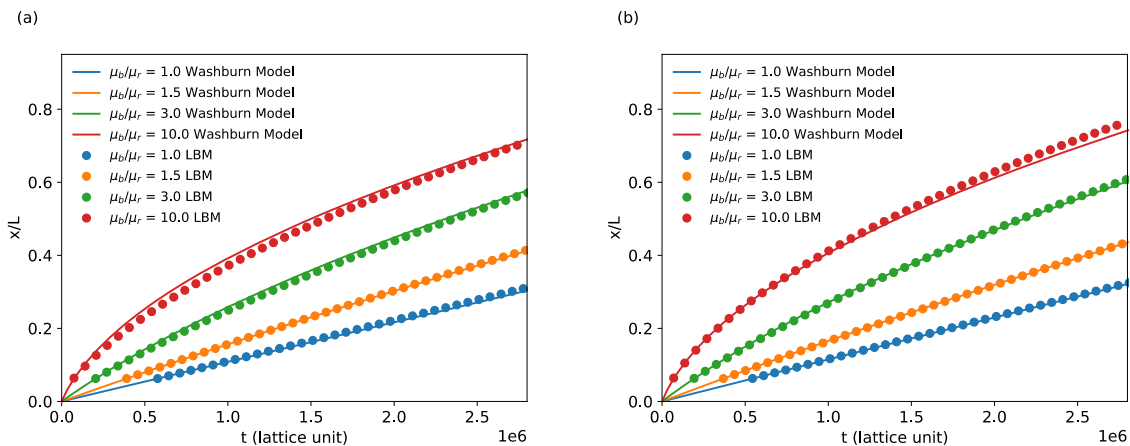


Fig. 3. The interface position of capillary rise as the function of time between two parallel plates: LBM simulation (dots) VS Washburn solution (lines). Both imbibition (a) and drainage (b) processes are considered. Gravity (i.e., $g = 0$) and inertial effects ($Re \approx 0.01$) is neglected. The height of the channel is 50 (lattice unit) and channel length is 800 (lattice unit). The viscosity ratio is 1.0, 1.5, 3.0, 10.0, respectively. The capillary number is 0.0015. The static contact angle for the wetting fluid is 60° .

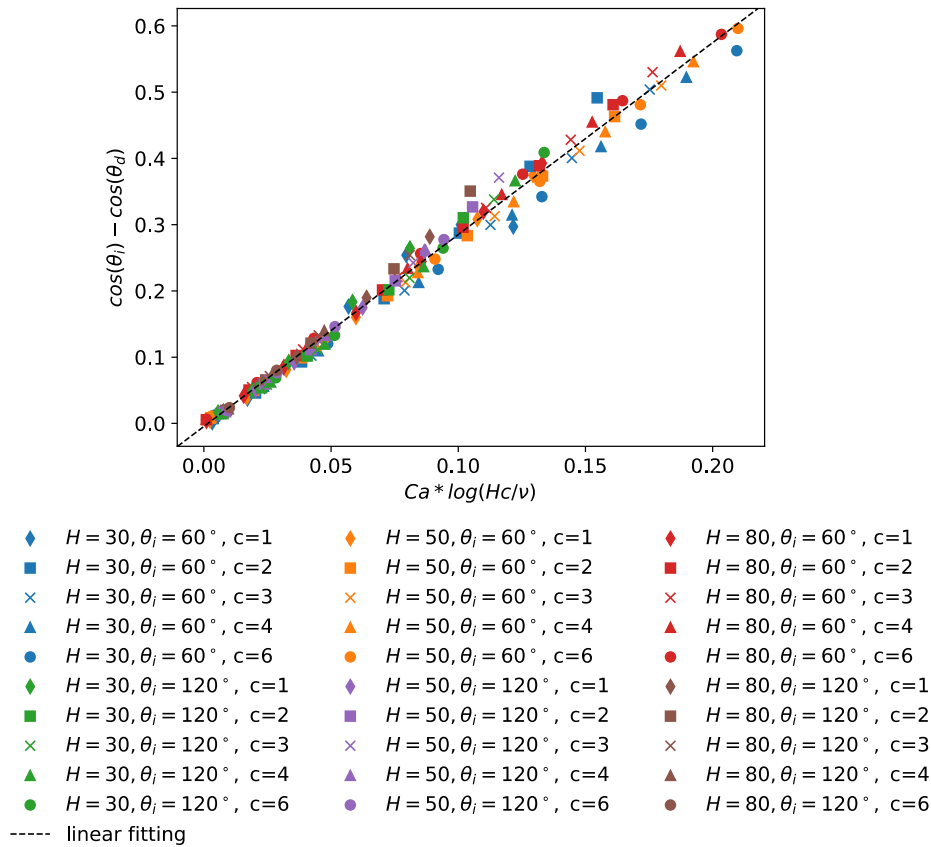


Fig. 4. The excessive curvature $\cos(\theta_i) - \cos(\theta_d)$ of different heights H and lattice speeds c and capillary numbers Ca scaled as the function of $Ca \ln(Hc/\nu)$. The different color denotes different channel height (H) and static contact angle (θ_i). The symbols denote different lattice speed c . The dashed line is the linear fitting of the result.

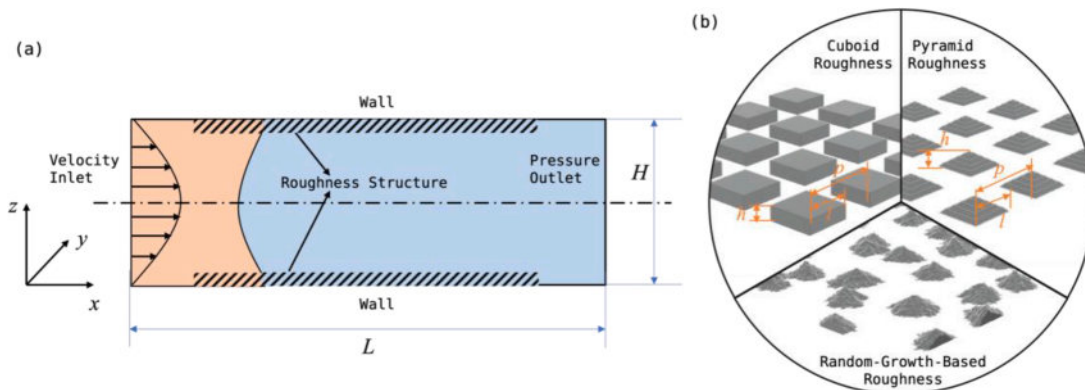


Fig. 5. (a) Illustration of the computation domain. The periodic boundary condition is applied at the y direction. The velocity boundary condition with a parabolic profile is applied at the inlet while pressure boundary is applied at the outlet, in order to maintain a steady advancing velocity at the interface as well as uniform pressure at the inlet and outlet. The computation domain is symmetric about $z = H/2$. The middle part of the channel is decorated with roughness. (b) Illustration of the roughness structures. The roughness is characterized by three parameters, the height h and the size l and period length a . The size l of random roughness is calculated via $l = a\sqrt{\phi}$, where ϕ denotes the ratio of the projection surface area of the roughness to the total surface area (hereafter).

Wang, Do-Quang [42] studied the droplet spreading process on surfaces decorated with micro-square pillars via experiments and phase-field simulations. Following Carlson, Bellani [43], they suggest that the effective contact-line friction is larger on rough surface than that on smooth surfaces. Mohammad Karim, Rothstein [44] studied the dynamic contact angle on the Teflon surfaces via the Wilhelmy plate experiments. Yang, Chen [37] performed numerical simulations via the phase field model on two-dimensional(2D) rough surfaces with groove

structures. They suggested that the hydrophobic characteristics could be obtained at the small capillary number Ca even if the surface was intrinsically hydrophilic. Some researchers also conducted simulations via LBM with similar 2D rough surfaces [45,46].

Nevertheless, 2D simulations conducted in the previous studies have a critical limitation, i.e., such simulations can only consider structures that are periodic perpendicular to the flow direction. Additionally, structures with square cross-section employed in the previous works

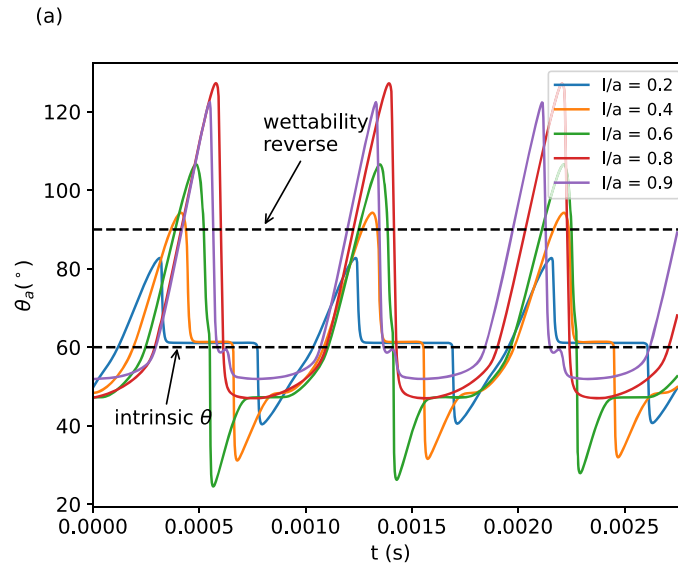


Fig. 6. Apparent contact angle θ_a as the function of displacing time on cuboid roughness with different roughness normalized size l/a . The normalized height h/H of the roughness structure is 0.1, $Ca = 0.001$.

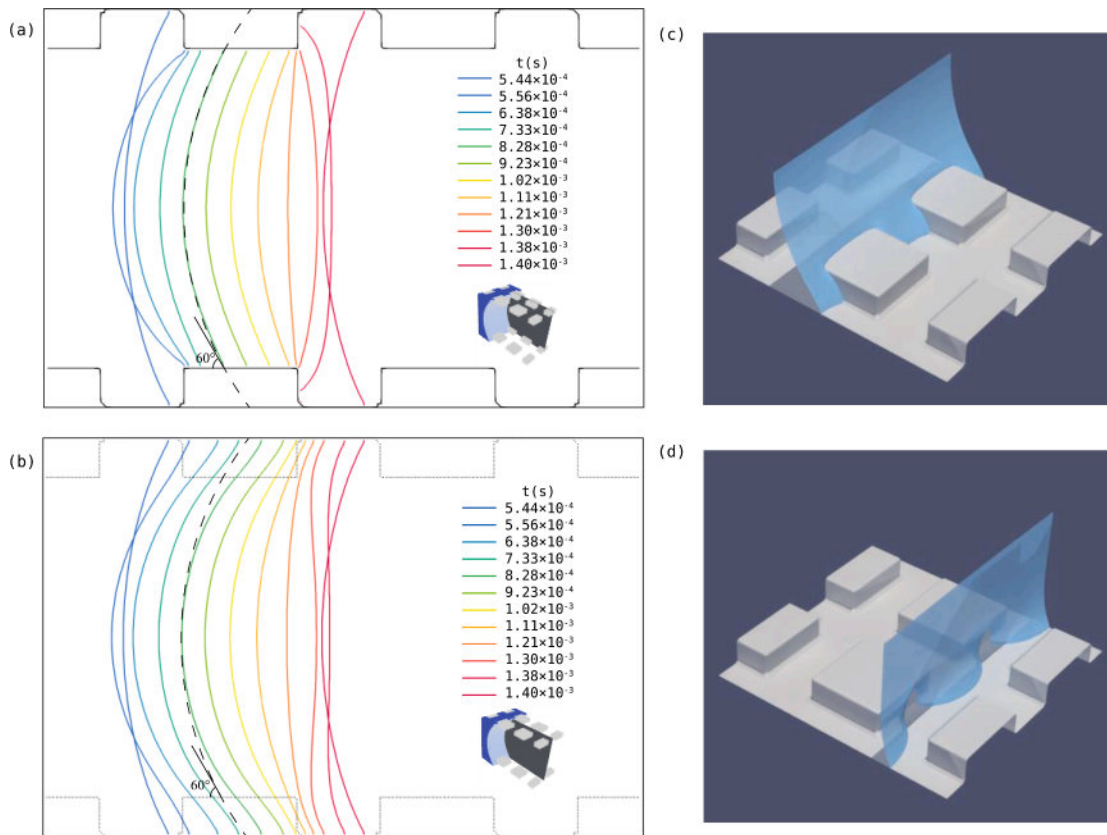


Fig. 7. (a, b) Cross-section view of the interface movement upon (a) and between (b) the cuboid roughness structures. The normalized height $h/H = 0.1$ and the normalized $l/a = 0.6$. The dashed line represents the meniscus with the intrinsic contact angle (60°) to the roughness structure. In comparison, the *invading precursor-films* induced by x-axis grooves are shown in (b). (c, d) Illustrations of the interface and three-phase contact line region as the contact line moves upon (c) and away (d) from roughness structures.

[37,42,45,46] induced a strong pin effect of the contact line at the square corners [37]. As a result, such results cannot be simply generalized to real rough surfaces, whose roughness shapes and distributions are random and heterogenous [47,48]. On the other hand, the high computational cost of the three-dimensional(3D) simulations is still one

of the major challenges. To the best of our knowledge, few studies have been reported on 3D simulations studying contact line movement on rough surfaces. Thus, the dynamic contact angle and contact line movement mechanisms on random surfaces remain largely to be explored.

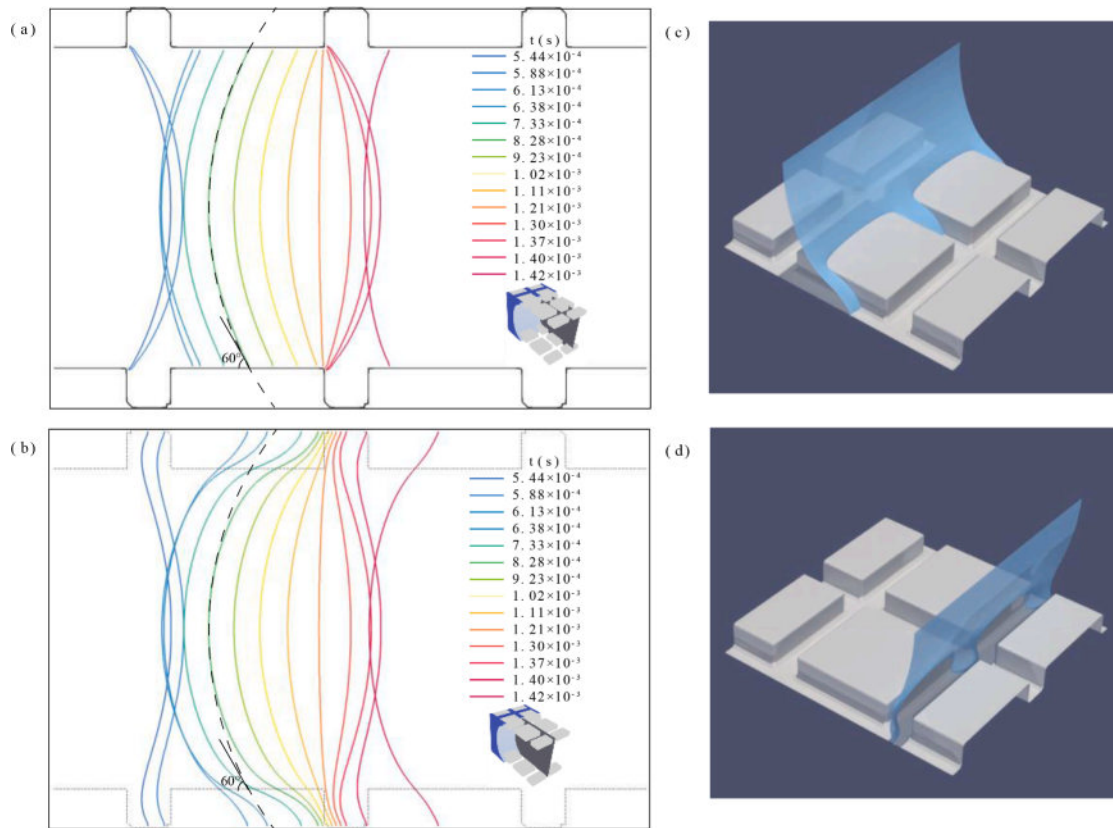


Fig. 8. (a, b) Cross-section view of the interface movement upon (a) and between (b) the cuboid roughness structures. The normalized height $h/H = 0.1$ and the normalized $l/a = 0.8$. The dashed line represents the meniscus with the intrinsic contact angle (60°) to the roughness structure. In comparison, the *invading precursor-films* induced by x-axis grooves are shown in (b). (c, d) Illustrations of the interface and three-phase contact line region as the contact line moves upon (c) and away (d) from roughness structures. Due to the smaller width of x-axis grooves, the *invading precursor-films* are much larger than those in Fig 7(b).

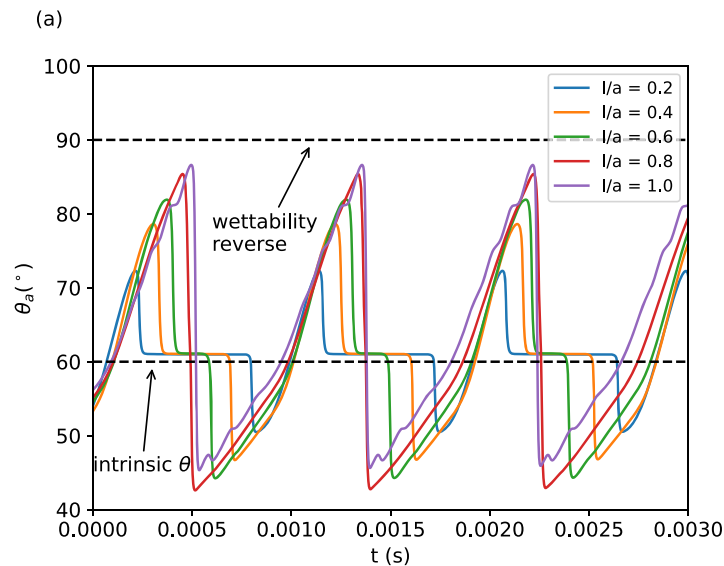


Fig. 9. Apparent contact angle as the function of time on pyramid roughness with different roughness normalized size l/a . The normalized height h/H of the roughness structure is 0.1, $Ca = 0.001$.

In this work, we employ the multiphase LBM to study dynamic contact angle on random surface roughness. The code is implemented in general-purpose graphics processing unit (GPGPU) via CUDA [49], which makes it possible to conduct high-performance 3D simulations. Numerical simulations are performed on surfaces which are decorated

with different kinds of roughness including a random-growth-based one. Unlike the 2D results, our results suggest that the surface remain hydrophilic during imbibition. The effects of shapes and sizes of roughness are studied. The rest of this paper is organized as follows. In Section 2, the multiphase LBM model and wetting boundary condition are

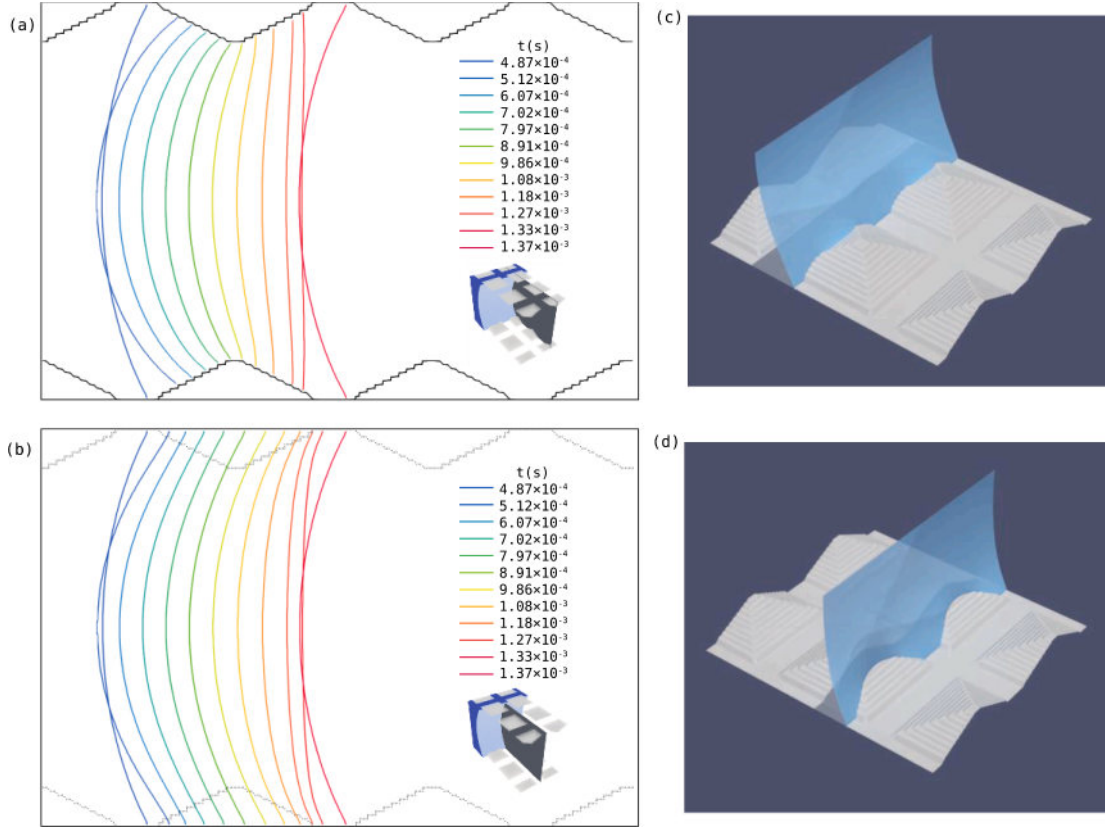


Fig 10. (a, b) Cross-section view of the interface movement upon (a) and between (b) the pyramid roughness structures. (c, d) Illustrations of the interface and three-phase contact line region as the contact line moves upon (c) and away (d) from roughness structures. The normalized height $h/H = 0.1$ and the normalized $l/a = 0.8$, $Ca = 0.001$.

introduced. In Section 3, we conduct 3 benchmarks to validate our model. Results and discussions are presented in Section 4. Last but not least, we summarize and provide conclusions in Section 5.

2. Model and method

2.1. CSF based color gradient model

In this work, we adopt the continuum-surface-force (CSF) scheme [50–52] of the color-gradient (CG) LBM as the solver for multiphase flows. The CG-CSF model is capable of adjusting interfacial and fluid properties independently, such as the surface tension, viscosity and interfacial thickness [53,54], making it one of the most popular multiphase LBM models [55,56]. In this model, the two immiscible fluids (red and blue) are represented by two sets of distribution functions f_i^b and f_i^r , where the subscripts i denotes the i th direction of the velocity \mathbf{e}_i in lattice models [27,57]. The total fluid distribution function is defined as $f_i = f_i^b + f_i^r$. The transportation of both fluids undergoes the following lattice Boltzmann equation:

$$f_i^k(\mathbf{x} + \mathbf{e}_i \delta t, t + \delta t) = f_i^k(\mathbf{x}, t) + \Omega_i^{2,k} [\Omega_i^1 + \bar{F}_i], \quad k = r, b, \quad (1)$$

where the superscript k represents either fluid b or fluid r . The collision operators Ω_i^1 , $\Omega_i^{2,k}$ and the source term \bar{F}_i are responsible for the viscous effect, the fluid separation, and the body force, correspondingly. The macroscopic variables are related to the distribution functions f_i^k via [58],

$$\rho^k = \sum f_i^k, \quad \rho^k \mathbf{u}^k = \sum f_i^k \mathbf{e}_i + \frac{\rho^k \mathbf{F}}{2}, \quad (2)$$

$$\rho = \sum_k \rho^k, \quad \rho \mathbf{u} = \sum_k \rho^k \mathbf{u}^k, \quad (3)$$

where ρ denotes the fluid density and \mathbf{u} denotes the fluid velocity.

In the CG-CSF model, the viscous collision operator Ω_i^1 is calculated collectively on the total distribution functions [56,59], i.e.,

$$\Omega_i^1 = -\frac{1}{\tau} (f_i - f_i^{eq}), \quad (4)$$

where τ is the relaxation time and f_i^{eq} is the equilibrium distribution function. In order to achieve better stability, accuracy and reduce the spurious velocities at interface [56,60], the LB multiple-relaxation-rate (MRT) framework [61,62] is employed. The LB equation with the MRT collision operator can be expressed as

$$f_i^k(\mathbf{x} + \mathbf{e}_i \delta t, t + \delta t) = f_i^k(\mathbf{x}, t) + \Omega_i^{2,k} \left[-\mathbf{M}^{-1} \mathbf{S} (\mathbf{M} \mathbf{f}(\mathbf{x}, t) - \mathbf{m}^{eq}) + \delta t \mathbf{M}^{-1} \left(\mathbf{I} - \frac{\mathbf{S}}{2} \right) \hat{\mathbf{F}} \right], \quad (5)$$

where \mathbf{f} denotes the vector form of the total distribution functions, and \mathbf{m}^{eq} stands for the equilibrium moment. Additionally, \mathbf{M} is the transformation matrix to the moment space and $\hat{\mathbf{F}} = \mathbf{M} \mathbf{f}$ accounts for the forcing term in the moment space. For the D3Q19 lattice [27] we adopted for 3D simulations, the equilibrium moments \mathbf{m}^{eq} and the forcing moments $\hat{\mathbf{F}}$ can be calculated via the macroscopic variables directly [27,63]

$$m^{eq} = \begin{bmatrix} \rho \\ -11\rho + 19\rho(u_x^2 + u_y^2 + u_z^2) \\ 3\rho - \frac{11}{2}\rho(u_x^2 + u_y^2 + u_z^2) \\ \rho u_x \\ -\frac{2}{3}\rho u_x \\ \rho u_y \\ -\frac{2}{3}\rho u_y \\ \rho u_z \\ -\frac{2}{3}\rho u_z \\ \rho(2u_x^2 - u_y^2 - u_z^2) \\ -\frac{1}{2}\rho(2u_x^2 - u_y^2 - u_z^2) \\ \rho(u_y^2 - u_z^2) \\ -\frac{1}{2}\rho(u_y^2 - u_z^2) \\ \rho u_x u_y \\ \rho u_y u_z \\ \rho u_x u_z \\ 0 \\ 0 \\ 0 \\ 0 \end{bmatrix}, \hat{F} = \begin{bmatrix} 0 \\ 38\mathbf{u}\cdot\mathbf{F} \\ -11\mathbf{u}\cdot\mathbf{F} \\ F_x \\ -\frac{2}{3}F_x \\ F_y \\ -\frac{2}{3}F_y \\ F_z \\ -\frac{2}{3}F_z \\ 2(2F_x u_x - F_y u_y - F_z u_z) \\ -(2F_x u_x - F_y u_y - F_z u_z) \\ 2(F_y u_y - F_z u_z) \\ -(F_y u_y - F_z u_z) \\ F_x u_x + F_y u_y \\ F_y u_y + F_z u_z \\ F_x u_x + F_z u_z \\ 0 \\ 0 \\ 0 \end{bmatrix} \quad (6)$$

and \mathbf{S} is a diagonal matrix composed of the relaxation parameters,

$$\mathbf{S} = \text{diag}(S_\rho, S_\epsilon, S_\epsilon, S_j, S_q, S_j, S_q, S_j, S_q, S_\nu, S_\pi, S_\nu, S_\pi, S_\nu, S_\nu, S_\nu, S_m, S_m, S_m), \quad (7)$$

According to Ref. [27], the following relaxation parameters are chosen in this work,

$$S_\rho = S_j = 0, \\ S_\epsilon = 1.19, S_\pi = S_\epsilon = 1.4, \\ \frac{1}{S_\nu} = \frac{3\nu}{c^2 \delta t} + \frac{1}{2}, S_m = S_q = \frac{8(2 - S_\nu)}{8 - S_\nu}. \quad (8)$$

In the CSF model, a body force \mathbf{F} is introduced which is responsible for the surface tension [52],

$$\mathbf{F} = \frac{1}{2}\sigma\kappa\mathbf{C}, \quad (9)$$

where σ is the surface tension, κ is the interfacial curvature and \mathbf{C} is the color gradient defined via the isotropic gradient operator proposed by Leclaire, Reggio [64],

$$\mathbf{C} = \nabla\phi = \frac{3}{\delta t} \sum_i \omega_i \mathbf{e}_i \phi(x + \mathbf{e}_i \delta t, t), \quad (10)$$

where ω_i denotes the weight coefficient in the D3Q19 lattice model, and $\phi = \frac{\rho_r - \rho_b}{\rho_r + \rho_b}$ is the order parameter indicating fluid types. With the color gradient \mathbf{C} , the interfacial curvature can be calculated via

$$\kappa = [(\mathbf{I} - \mathbf{nn}) \cdot \nabla] \cdot \mathbf{n}, \quad (11)$$

where \mathbf{n} denotes the normal direction of the color gradient \mathbf{C} ,

$$\mathbf{n} = \frac{|\nabla\phi|}{\nabla\phi}. \quad (12)$$

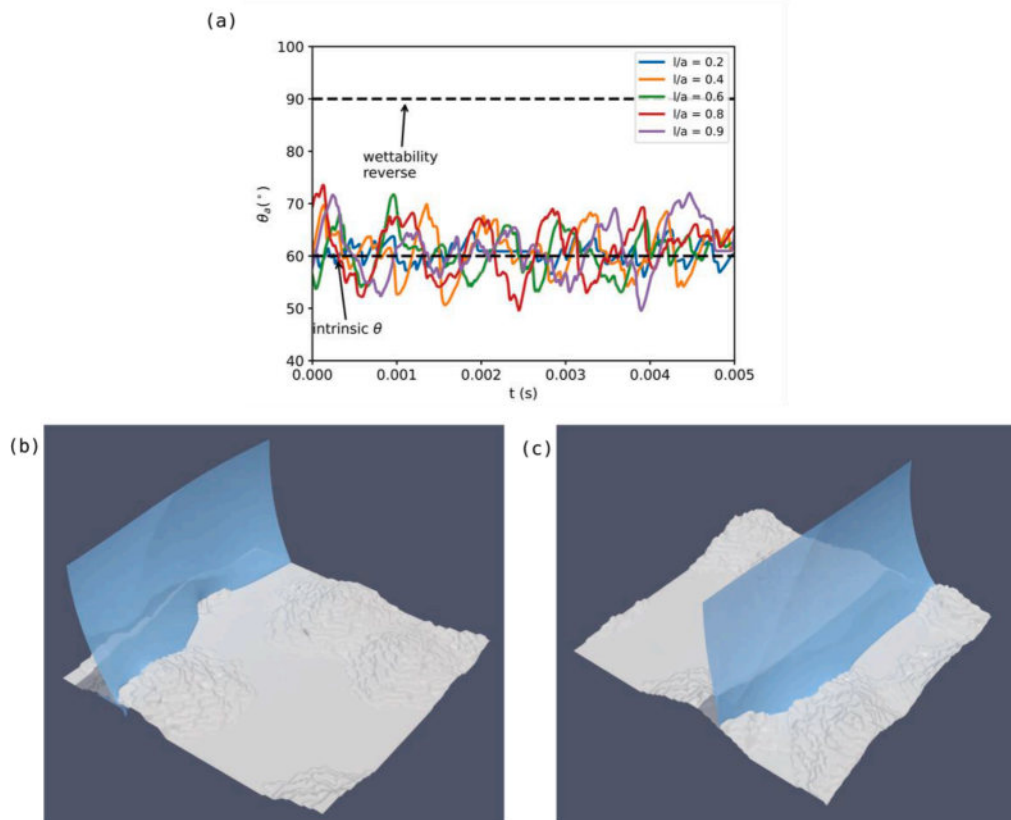


Fig. 11. (a) Apparent contact angle as the function of time random-growth-based roughness (b, c) Illustrations of the interface and three-phase contact line region on random roughness structures. The normalized height $h/H = 0.1$ and the normalized $l/a = 0.8$, $Ca = 0.001$.

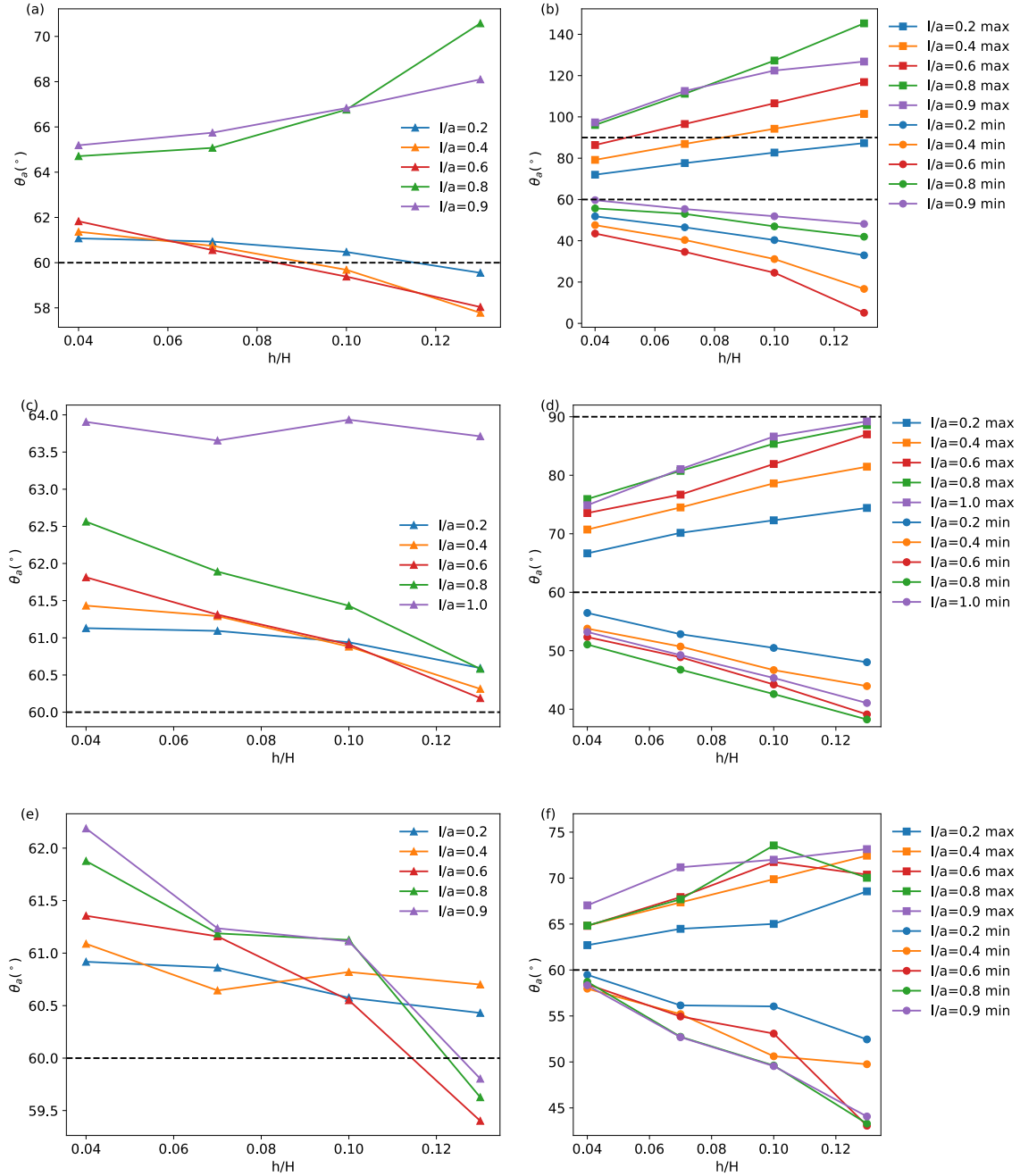


Fig. 12. The average apparent contact angle (a, c, e) and maximum and minimum apparent contact angle (b, d, f) as the function of the normalized height h/H . From top to bottom: cuboid roughness: (a, b), pyramid roughness: (c, d), random roughness: (e, f). $Ca = 0.001$.

Finally, a recoloring step is employed to separate the two fluids as the collision operator $\Omega_i^{2,k}$, which can be expressed as [53],

$$f_i^{++k}(\mathbf{x}, t) = \frac{\rho^k}{\rho} f_i^+ \pm \beta \frac{\rho_b \rho_r}{\rho} \cos(\psi_i), \quad (13)$$

where

$$\cos(\psi_i) = \frac{|\mathbf{e}_i \cdot \mathbf{C}|}{|\mathbf{e}_i| |\mathbf{C}|}, \quad (14)$$

where \mathbf{C} is the color gradient defined by Eq. (10). f_i^+ denotes the post-collision distribution function, while f_i^{++k} denotes the pre-streaming distribution function. Then f_i^{++k} streams to the nearby lattice nodes separately following Eq. (1).

2.2. Wetting boundary condition

In this work, we adopt the geometry-based wetting model proposed in Akai, Bijeljic [65]. First suggested by Xu, Liu [56], geometry-based wetting model can significantly reduce the spurious velocities and prevent the unphysical mass transport at the fluid boundary nodes [65,66] compared to the fictitious-density model [67]. This is achieved by directly modifying the interface normal vector \mathbf{n} to the desired contact angle via solving

$$\mathbf{n}_{\pm} = \left(\cos \pm \theta - \frac{\sin \pm \theta \cos \theta'}{\sin \theta} \right) \mathbf{n}_s + \frac{\sin \pm \theta}{\sin \theta'} \mathbf{n}^*, \quad (15)$$

$$\theta' = \arccos(\mathbf{n}_s \cdot \mathbf{n}^*),$$

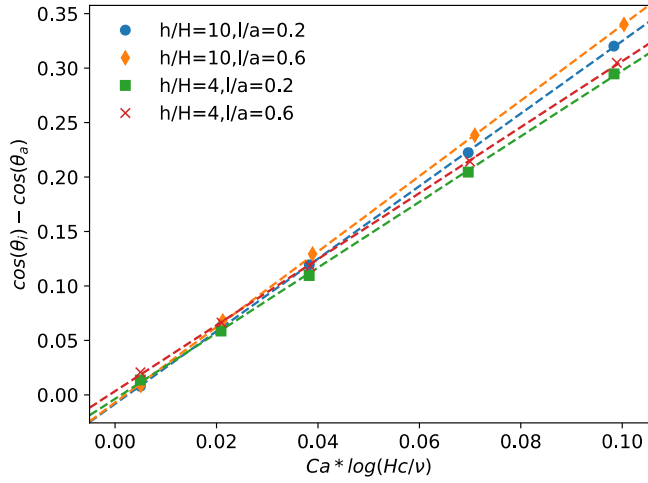


Fig. 13. The excess curvature $\cos(\theta_i) - \cos(\theta_a)$ as the function of $Ca \ln(Hc/\nu)$ on random roughness of different roughness heights and sizes. The dots are simulation results, while the lines are the linear fittings. The results are similar for other roughness parameters and roughness shapes.

where θ denotes the contact angle, \mathbf{n}_s is the unit normal vector of boundary and \mathbf{n}^* is the estimated interfacial direction via Eq. (12). Then \mathbf{n}^* is altered to one of \mathbf{n}_+ and \mathbf{n}_- which has the shorter Euclidean distance to \mathbf{n}^* , with the color gradient C modified correspondingly. For complex geometries, \mathbf{n}_s can be calculated following Ref. [56]. As a result, the wetting model is introduced via the interfacial force according to Eqs. (9) and (11).

Besides the adjustment of the interface normal vectors, minimizing the spurious velocities at the three-phase contact line region requires two crucial steps [60,68]: the extrapolation of the order parameter ϕ and the extrapolation of the interface normal vectors \mathbf{n} , which reduces the color gradient at boundary, and consequently reduces the interactions between the fluid boundary nodes and the solid boundary nodes according to Eqs. (9) and (11).

2.3. Parallel implementation

To overcome the challenge of 3D simulations, the LBM-CG-CSF model is ported to general-purpose graphics processing unit (GPGPU) via CUDA [49,60]. The direct-addressing-based AA pattern and if-else branch is adopted to treat complex structures while the wetting boundary condition is treated by indirect addressing. With the high computation power and the memory bandwidth provided by the modern GPGPUs, our implementation reaches 800 MLUPS (million lattice updates per second) on Nvidia Tesla V100 and 1100 MLUPS on Nvidia A100, which makes it practical to resolve finer roughness structures as well as conduct 3D simulations.

3. Model validation

To validate our model, several benchmarks have been conducted. The first benchmark is the stationary droplet test which validates the code by the Young-Laplace equation. Initially, a cubic droplet with a given side length is placed at the center of the computational domain. The droplet deforms to a sphere due to the surface tension at the equilibrium state as Fig 1(a) demonstrates. The pressure difference across the interface can be described by the Young-Laplace equation,

$$\Delta p = \sigma \left(\frac{1}{R_1} + \frac{1}{R_2} \right) = \frac{2\sigma}{R}, \quad (16)$$

where Δp , σ and R denotes the pressure difference, the surface tension and the radius of the droplet, respectively. A cubic domain of $200 \times 200 \times 200$ with the periodic boundary conditions for all the bound-

aries. Cubic bubbles with side length of 20 to 70 is placed at the center of the domain initially. The surface tension is set as 0.03. As Fig. 1(b) shows, our simulation results agree well with the theory.

In the second case, we validate the wetting model by simulating droplets attached to the wall. Similar to the previous one, a stationary droplet with a radius of 30 is placed attached to the wall initially. At the steady state, the droplet deforms to a certain contact angle corresponding to the wetting boundary condition. Since the shape of the droplet is a part of sphere, ignoring gravity, in the benchmark, the radius and the center of each sphere can be calculated by extracting and fitting [69] all interfacial points defined via $|\phi| < 0.9$. As Fig. 2(a) shows, the static contact angle can be calculated via

$$\cos(\theta_c) = -\frac{y_c}{R}, \quad (17)$$

where y_c and R denotes the y-coordinate of the center and the radius of the sphere, respectively. Fig. 2(c) illustrates that the measured contact angles agree well with the desired contact angles for a wide range of contact angles. Current results are comparable with [54,60,65] in accuracy.

Apart from the aforementioned benchmarks which mainly examines the interfacial dynamics at stationary state, we also conduct a capillary rise test. Consider a flow channel consists of two parallel plates which is initially filled with fluid r . The inlet and outlet of the channel is connected to the fluid b and the fluid r reservoirs with constant pressure p_{in} and p_{out} , respectively. The fluid r will be displaced by the fluid b due to the pressure difference, $\Delta p = p_{in} - p_{out}$ and capillary force. Neglecting gravity (i.e., $g = 0$) and inertial effects (i.e., $Re \ll 1$), which is usually valid at micro and nano scale, the interface position can then be determined via the Washburn model [11],

$$x(t) = \frac{H^2}{12\mu_b} \frac{\Delta p - p_c}{L} t, \quad (\mu_b = \mu_r) \quad (18)$$

$$x(t) = \frac{\mu_r L}{\mu_b - \mu_r} + \frac{\sqrt{36\mu_r^2 L^2 + 6H^2(\Delta p - p_c)(\mu_b - \mu_r)t}}{6(\mu_b - \mu_r)}, \quad (\mu_b \neq \mu_r) \quad (19)$$

where H and L denotes channel height and length, respectively. μ_b and μ_r represents the viscosity of the fluid b and the fluid r . The capillary pressure p_c can be determined by the Young-Laplace equation,

$$p_c = \frac{2\sigma \cos\theta}{H}. \quad (20)$$

To minimize the influence of the dynamic contact angle and inertial force, we let $Re_b = (\rho_b H u_m) / \mu_b \sim 0.01$, $Ca_b = \mu_b u_m / \sigma \sim 10^{-3}$, $\mu_b \geq \mu_r$ and the density ratio $\rho_b / \rho_r = 1$. The u_m is the mean velocity in the case where the viscosity ratio $\mu_b / \mu_r = 1$. Both the imbibition (non-wetting fluid displaced by wetting fluid) and drainage (wetting fluid displaced by non-wetting fluid) process are considered and the static contact angle of the wetting fluid is 60° . In this benchmark, we let $Re_b \approx 0.01$ and $Ca_b = 0.0015$. The height of the channel is 50 (lattice unit) and channel length is 800 (lattice unit). As Fig. 3 shows, our simulation results agree well with the Washburn Model at different viscosity ratios.

The dynamic effect on contact angle is also studied by varying the capillary number ($Ca = 10^{-4} \sim 10^{-1}$). To simplify the problem, we set the viscosity ratio to 1. Similarly, gravity (i.e., $g = 0$) and inertial effects (i.e., $Re = 0.005$) are neglected. Once the Ca and Re are set, the fluid viscosity and the estimated velocity can be uniquely determined via

$$v = \sqrt{\frac{Ca\sigma H}{Re\rho}}, \quad (21)$$

$$u = \sqrt{\frac{CaRe\sigma}{H\rho}}. \quad (22)$$

Then the inlet pressure can be calculated via Eq. (18). Although via

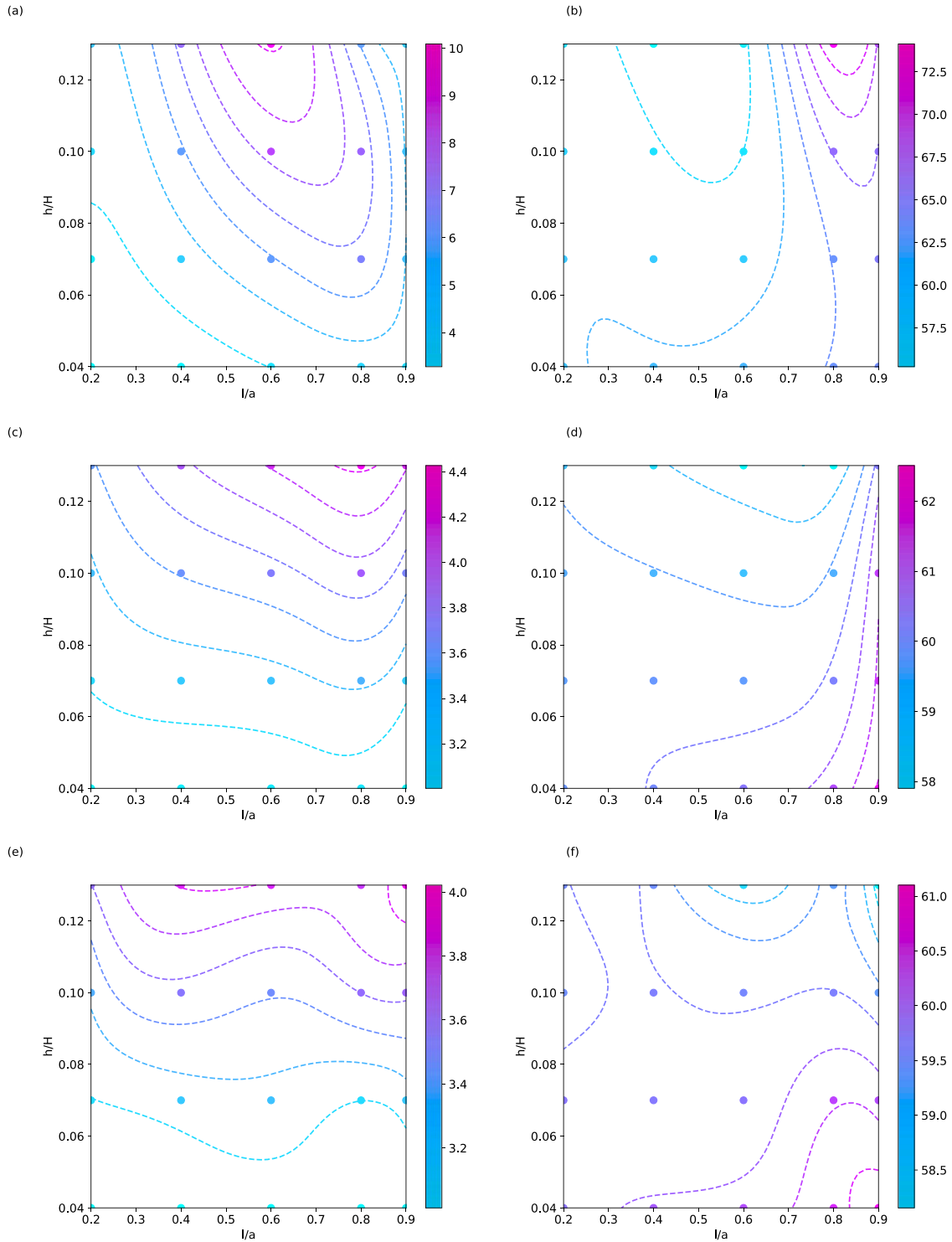


Fig. 14. The slope K (a, c, e) and apparent contact angle $\theta_{a,0}$ at extremely low Ca (b, d, f) as the function of the normalized height h/H and the normalized size l/a . The points are simulation results and contours (lines) are obtained via interpolation. From top to bottom: cuboid roughness: (a, b), pyramid roughness: (c, d), random roughness: (e, f).

this procedure, the simulated velocity is different from the prescribed one, the difference in Re and Ca is small. Additionally, the simulated Ca is used in further analysis. The dynamic contact angle is measured via adjusting the contact angle in the Washburn Model (Eq. (18) and Eq. (20)) to find the best match between simulation and theory. As Fig. 4 shows, the excess curvature $\cos(\theta_i) - \cos(\theta_d)$ linearly depends on $Ca \ln(H/l_s)$, where l_s is the slip length, θ_i and θ_d represent the intrinsic and dynamic contact angle respectively. This is consistent with the

hydrodynamic model [12,14] when the density ratio and the viscosity ratio is 1. As for CG LBM, Latva-Kokko and Rothman [28] suggest that the slip length l_s is proportion to the kinetic viscosity ν and related to microscopic parameters in LBM. Based on dimensional analysis, we find that the slip length $l_s = \nu/c$, where c denotes the lattice speed, i.e.,

$$\cos(\theta_i) - \cos(\theta_d) = 2.86Ca \ln \frac{Hc}{\nu}. \quad (23)$$

This could be explained that the mobility of the interface is

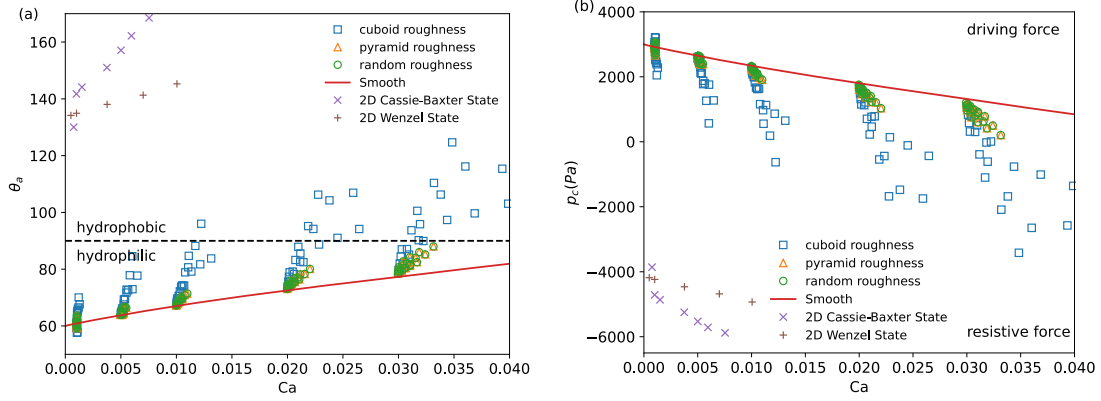


Fig. 15. (a) The apparent contact angle θ_a as the function Ca : 3D roughness surfaces VS 2D roughness surfaces VS smooth surfaces. The surface is intrinsically hydrophilic ($\theta_s = 60^\circ$). The smooth result is Eq. (23). The results of 2D roughness surfaces (2D Cassie-Baxter State and 2D Wenzel State) are from Yang, Chen [37], which suggests strong wettability reverse. Such results are difficult to find on 3D roughness. (b) The typical capillary force in micro-tubes. Data is reorganized considering the capillary force a micro-tube with a radius of $10 \mu\text{m}$ and the surface tension is 0.03 N/m .

influenced by the lattice speed c , which further influences the slip length [70]. The present results prove that the geometry-based wetting model with CSF based CG model spontaneously captures the dynamic nature of the contact angle. To the best of our knowledge, we are the first to provide the correlation for slip length in multiphase LBM. Although the simulation results of this benchmark are in lattice unit, the conclusion can be generalized to perform non-lattice unit simulations.

4. Results and discussion

4.1. Numerical setup

As Fig. 5(a) shows, the two-phase fluid displacement between two parallel plates decorated with the surface roughness is studied. In other words, the periodic boundary condition is applied at the y direction, which allows us to analysis the flow via the two-dimensional Washburn model. The velocity boundary condition with a parabolic profile is applied at the inlet while pressure boundary is applied at the outlet, in order to maintain a steady advancing velocity at the interface as well as uniform pressure at the inlet and outlet. Thus, the apparent contact angle θ_a can be calculated via,

$$\cos(\theta_a) = \frac{H}{2\sigma} (p_{out} - p_{in} + p_{vis}) \quad (24)$$

where p_{in} , p_{out} and p_{vis} denotes for the inlet pressure, the outlet pressure and the pressure drop due to the viscous effect. The p_{in} , p_{out} can be monitored directly at the inlet and the outlet, while the p_{vis} is obtained by simulating the corresponding single-phase case.

Since we mainly consider the imbibition process in micro and nano channels, only non-wetting phase displaced by the wetting phase is simulated. The height of the channel is fixed as $8 \mu\text{m}$. The length and the width of the channels depends on the roughness pattern of the surface. A grid size of $0.08 \mu\text{m}$ is employed for all simulations. Similar to the benchmark, the displacing process can be described two non-dimensional number, i.e., the capillary number Ca and Reynold's number Re . With a given set of Ca and Re , the inlet velocity and the viscosity of the fluid can be determined via Eqs. (21) and (22). We adopt $Re \approx 0.005$, $Ca \approx 10^{-3} \sim 10^{-1}$ and the densities of all fluids are 1000 kg/m^3 unless otherwise specified.

To make our analysis manageable, three types of surface roughness are considered in this work, i.e., cuboid roughness, pyramid roughness and random-growth-based roughness [33], as Fig. 5(b) shows. We assume that all roughness structures have has good isotropy and homogeneity.

4.2. Contact line movement at low Ca

We first present the apparent contact angle results on the cuboid surface since the corresponding 2D groove-like structure has been widely investigated [37,46,71]. Fig. 6 shows the apparent contact angle as the function of the displacing time when $Ca = 0.001$ with different normalized size l/a . It can be observed that the transient apparent contact angle oscillates periodically which is also observed in 2D simulations [37]. However, unlike the 2D groove-like structures, the present results not only demonstrate the structure-induced wettability reverse [37,46], but also reveal the structure-induced hydrophilic enhancement. This is because of the grooves along the advancing direction x axis (x -axis grooves, hereafter), while in the 2D simulations, grooves are all perpendicular to the advancing direction (y -axis grooves, hereafter).

To analyze the variation of apparent contact angle, the interface movement on the cuboid roughness surface is displayed in Figs 7 and 8. For cases with $l/a \leq 0.6$, i.e., the roughness forms a sparse pattern. The θ_a remain the intrinsic contact angle when the contact line moves at the smooth region as Fig 7 shows. When the interface approaches the roughness, on the one hand, since the contact line moves upwards, the effective channel height is decreased, resulting in smaller apparent contact angle. For the convenience of description, we name this phenomenon **radius reduction**. Meanwhile, the upward movement of the contact line is much faster than the forward movement of the central meniscus, which further effectively bend the main meniscus and reduces the apparent contact angle at the early stage, named as **central meniscus lag**. In our simulations, the central meniscus even moves backwards slightly as the fluid at corners is pushed to the center. On the other hand, as Fig 7(b) shows, the x -axis grooves which have smaller width induces a larger capillary force locally, resulting precursor-films which could also bend the main meniscus and enhance hydrophilic (**invading precursor-films**). The the x -axis grooves also reduce the maximum apparent contact angle. As the contact line leaves the roughness structure, the contact line at the grooves moves advance with the main meniscus, forming **departure precursor-films** as Fig 7(b, c) show. In contrast, in 2D simulations, the contact line is pinned at the roughness edge till $\theta_a = \pi/2 - \theta_i$, similar to Fig 7(a). Therefore, the present results have smaller maximum θ_a compared to 2D results [37].

However, as Fig 8 shows, for $l/a \geq 0.8$, a smaller channel width of the micro-grooves resulting a higher capillary pressure, which enhances the **invading-precursor films**. On the other hand, larger cuboid blocks increase the pin effect of the contact line. The main meniscus reaches the next roughness structure before the contact line completely detach the previous structure as Fig 8(b) demonstrates. Therefore, **central meniscus lag** is not observed in such cases, which could explain the different

pattern of enhanced hydrophilic between $l/a \leq 0.6$ and $l/a \geq 0.8$ demonstrate in Fig 6. Aforementioned two patterns are similar to the *stick-slip pattern* and the *stick-jump-slip pattern* observed in 2D simulations [37]. However, the present results are all in Wenzel state while two-dimensional simulations suggest a Wenzel state for the stick-slip pattern and a Cassie-Baxter state for the stick-jump-slip pattern, which could be explained by *departure-precursor films* induced by 3D structures.

Figs. 9 and 11 show the apparent contact angle as the function of time on pyramid roughness and random-growth-based roughness. For the pyramid roughness, the apparent contact angle oscillates periodically, which is consistent with the cuboid roughness. Nevertheless, the amplitudes of the oscillations on pyramid roughness are much smaller than those on cuboid roughness surface, which could suggest a smaller contact angle hysteresis. On the one hand, the gentle increase of the roughness height weakens the *radius reduction* and *central meniscus lag*, which reduces the hydrophilic enhancement. On the other hand, the pin effect of the pyramidal structure on the contact line is also weaker, which reduces the maximum θ_a . As a matter of fact, for a 2D triangular roughness, the apparent dynamic contact angle can be view as $|\theta_i - \theta_s|$ when contact line approaches roughness and $\theta_i + \theta_s$ when the contact line departs the roughness, where θ_s denotes the structural angle [72]. This mechanism (*slope effect*) also plays a role for 3D pyramid roughness while affected by 3D meniscus as Fig 10(c, d) shows. Wettability reverse and *stick-jump-slip pattern* does not appear on the pyramid roughness. For random rough structures, the oscillations of the apparent contact angle exhibit an irregular characteristic, which are caused by the irregular spatial distribution of the structure itself. Additionally, an irregular spatial distribution also destroys the cooperative effect of the aligned structures according to Fig 11(c, d), resulting smaller amplitude of the oscillations around the intrinsic contact angle compared to pyramid roughness.

4.3. Height effect

We also study the height effect of the roughness structure as Fig. 12 shows. With a larger roughness height, the effective channel width is decreased and the influence of the micro-grooves is increased, which enhances the *radius reduction*, the *central meniscus lag* and the *invading-precursor films* for cuboid roughness and the *slope effect* for pyramid roughness and random roughness. As a result, the maximum apparent contact angle increases when the roughness height increases while the minimum apparent contact angle is exactly the opposite for all roughness types and size. The present results also indicate that larger roughness heights result in larger oscillating amplitude of the apparent contact angle. Additionally, except for the cuboid roughness, most maximum apparent contact angles are below 90° , which suggests that wettability reverse is difficult to occur in 3D roughness structures.

As for the average apparent contact angle, under most of the circumstances, the increase of the roughness height enhances the hydrophilic, which indicates the hydrophilic enhancement is more sensitive to height than the hydrophilic diminution. For cuboid roughness with $l/a \geq 0.8$, the apparent contact angle increases with the increase of roughness height, which could be due to the *stick-jump-slip pattern* in those cases rather than *stick-slip pattern* in other cases. The variation of the apparent contact angle due to roughness height is 4° , suggesting roughness height is insignificant in terms of the average apparent contact angle.

For static contact angle in Wenzel states, the apparent contact angle follows Wenzel [35], $\cos(\theta_a) = r^* \cos(\theta_i)$, where r^* is the roughness parameter. As $r^* > 1$ is valid for all roughness surface, the apparent contact angle should be smaller than intrinsic contact angle. As a result, the present results also suggest that the Wenzel model is not valid for dynamic contact angle due to the contact line movement.

4.4. Velocity effect

In this section, we consider the velocity effect on wettability on roughness surface. The contact line motions are similar to those at low Ca number. Firstly, as Fig. 13. shows, the excess curvature $\cos(\theta_i) - \cos(\theta_a)$ also linearly depends on $Ca \ln(Hc/\nu)$ on random roughness surfaces, which is also the case for pyramid roughness surface and cuboid roughness. Thus, the apparent contact angle on rough surfaces follows

$$\cos(\theta_i) - \cos(\theta_a) = K(l/a, h/H)Ca \ln\left(\frac{Hc}{\nu}\right) + b(l/a, h/H), \quad (25)$$

where $K(l/a, h/H)$ denotes the structural effect on the slope (sensitivity) of the excess curvature as the function of $Ca \ln(Hc/\nu)$, while $b(l/a, h/H)$ denotes the structural effect on the advancing contact angle $\theta_{a,0}$ at extremely low Ca . $\theta_{a,0} = \arccos(\cos(\theta_i) - b)$.

The results of different roughness heights and sizes on different structures are displayed in Fig. 14. It can be observed that the slopes K of all 3 roughness types are higher than that of smooth surfaces, which indicates that the apparent contact angle θ_a increases faster with the increase of the capillary number Ca on rough surfaces than that on smooth surfaces. This is consistent with the experimental results in [42, 43]. In their works, effect of the roughness surface is modeled as the increase of viscosity μ_{eff} , resulting $Ca_{eff} > Ca$, in other words, the larger slope K . In contrast, it is obtained that the slip length l_s is increased in 2D simulations, indicating a smaller slope [37].

The slopes of cuboid roughness surfaces are much higher than that of other roughness surfaces, which is due to the contact line movement analyzed in Section 4.1. Generally speaking, with larger structure height, induces stronger effect on the contact line movement, resulting in the larger slope K , which is also observed in experiments [42]. However, our results suggest that structure size effect on the slope K is not monotonic. The maximum slope is obtained at relatively large structure size, because different mechanism is affected by structure size differently. The structure size effect is further influenced by the heterogeneity of the roughness distribution comparing random roughness (Fig. 15(e)) and regular roughness (Fig. 15(a) and (c)).

As for the apparent contact angle $\theta_{a,0}$ at extremely low Ca , the maximum $\theta_{a,0}$ is obtained at the small roughness height and the large roughness size for the pyramid roughness and the random roughness. Nevertheless, due to the *stick-jump-slip pattern* on cuboid roughness, the maximum $\theta_{a,0}$ is observed at the large roughness height and the large roughness size. The value of the maximum $\theta_{a,0}$ is also much larger than that of the pyramid roughness and the random roughness.

Finally, we present a direct comparison among 3D roughness surfaces, 2D roughness surfaces [37] and smooth surfaces. We can observe that with 2D roughness surfaces in 2D simulations, the apparent contact angle is overestimated in both Wenzel State and Cassie-Baxter state. Even at a small Ca , the apparent contact angle θ_a is hydrophobic though the surface is hydrophilic with the intrinsic contact angle $\theta_i = 60^\circ$. On the other hand, the apparent contact angle θ_a is underestimated by about 25% at relatively large Ca on the smooth surface compared to random roughness. Interestingly, the apparent contact angle predicted on the pyramid surface is close to that predicted on the random roughness due to the similarity in the pyramid shape and the peak shape in random roughness, which indicates that the similarity in morphology may produce similar results.

5. Conclusions

We have investigated the surface roughness effects in this work on dynamic wetting in imbibition processes in microchannels via 3D direct simulations by GPU-LBM. Three types of surface roughness have been considered, i.e., the cuboid one, the pyramid one and the random-growth-based roughness. The effects from roughness size and

imbibition velocity have been studied on the dynamic contact angle, and compared with the results of the corresponding 2D one. The apparent contact angle oscillates because of roughness structures as the interface advances, which is also observed in the 2D simulations. The amplitude of oscillation is strongly influenced by the roughness shape. However, at a small capillary number, the rough surfaces remain hydrophilic due to the weaker pin-effect of the 3D structure. For all the roughness conditions we consider, the flow remain the Wenzel State though the stick-jump-slip or the stick-slip motion [37] can be similarly observed in the 3D roughness structures as well. In contrast to the wettability alternation in 2D simulations, the 3D rough surfaces remain hydrophilic and Wenzel state at even low capillary numbers for hydrophilic surfaces. The results also indicate that the 2D simplifications overestimate the pressure drop for rough channels, while underestimate over 20% for smooth channels. Hence, it is of great significance to consider 3D roughness for dynamic wetting in real microchannels.

Declaration of Competing Interest

The authors declare that they have no known competing financial interests or personal relationships that could have appeared to influence the work reported in this paper.

Acknowledgments

This work is financially supported by the National Key R&D Program of China [2019YFA0708704] and the NSF grant of China [12272207].

References

- Zheng J, et al. Characterization of spontaneous imbibition dynamics in irregular channels by mesoscopic modeling. *Comput Fluids* 2018;168:21.
- Huang J, Xiao F, Yin X. Lattice Boltzmann simulation of pressure-driven two-phase flows in capillary tube and porous medium. *Comput Fluids* 2017;155:134.
- Morrow NR, Mason G. Recovery of oil by spontaneous imbibition. *Curr Opin Colloid Interface Sci* 2001;6(4):321.
- Chang C, et al. Pore-scale supercritical CO₂ dissolution and mass transfer under imbibition conditions. *Adv Water Resour* 2016;92:142.
- Peng X, et al. Lab-on-a-chip systems in imbibition processes: a review and applications/issues for studying tight formations. *Fuel* 2021;306:121603.
- Zhu Y, Petkovic-Duran K. Capillary flow in microchannels. *Microfluid Nanofluidics* 2009;8(2):275.
- Xue HT, et al. Contact angle determined by spontaneous dynamic capillary rises with hydrostatic effects: experiment and theory. *Chem Phys Lett* 2006;432(1–3):326.
- Girardo S, et al. Interplay between shape and roughness in early-stage microcapillary imbibition. *Langmuir* 2012;28(5):2596.
- Li X, et al. An experimental study on dynamic pore wettability. *Chem Eng Sci* 2013;104:988.
- Hamraoui A, et al. Can a dynamic contact angle be understood in terms of a friction coefficient? *J Colloid Interface Sci* 2000;226(2):199.
- Washburn EW. The dynamics of capillary flow. *Phys Rev* 1921;17(3):273.
- Sheng P, Zhou M. Immiscible-fluid displacement: contact-line dynamics and the velocity-dependent capillary pressure. *Phys Rev A* 1992;45(8):5694.
- Voinov OV. Hydrodynamics of wetting. *Fluid Dyn* 1976;11(5):714.
- Cox RG. The dynamics of the spreading of liquids on a solid surface. Part 1. Viscous flow. *J Fluid Mech* 1986;168:169.
- Blake TD, Haynes JM. Kinetics of liquid-liquid displacement. *J Colloid Interface Sci* 1969;30(3):421.
- Petrov P, Petrov I. A combined molecular-hydrodynamic approach to wetting kinetics. *Langmuir* 1992;8(7):1762.
- Jacqmin D. Contact-line dynamics of a diffuse fluid interface. *J Fluid Mech* 2000;402:57.
- van Mourik S, Veldman AEP, Dreyer ME. Simulation of capillary flow with a dynamic contact angle. *Microgravity - Sci Technol* 2005;17(3):87.
- Dupont J-B, Legendre D. Numerical simulation of static and sliding drop with contact angle hysteresis. *J Comput Phys* 2010;229(7):2453.
- Deganello D, et al. Numerical simulation of dynamic contact angle using a force based formulation. *J Nonnewton Fluid Mech* 2011;166(16):900.
- Hong SD, Ha MY, Balachandar S. Static and dynamic contact angles of water droplet on a solid surface using molecular dynamics simulation. *J Colloid Interface Sci* 2009;339(1):187.
- Nie XB, et al. A continuum and molecular dynamics hybrid method for micro- and nano-fluid flow. *J Fluid Mech* 2004;500:55.
- Yang C, Tartaglino U, Persson BN. Influence of surface roughness on superhydrophobicity. *Phys Rev Lett* 2006;97(11):116103.
- Li H, et al. Dynamic contact angles and mechanisms of motion of water droplets moving on nanopillared superhydrophobic surfaces: a molecular dynamics simulation study. *Langmuir* 2018;34(34):9917.
- Li Q, et al. Lattice Boltzmann methods for multiphase flow and phase-change heat transfer. *Prog Energy Combust Sci* 2016;52:62.
- Huang H, Sukop M, Lu X. Multiphase lattice Boltzmann methods: theory and application. UK: John Wiley & Sons; 2015.
- Krüger T, et al. The lattice Boltzmann method: Principles and Practice. Switzerland: Springer; 2017.
- Latva-Kokko M, Rothman DH. Scaling of dynamic contact angles in a lattice-Boltzmann model. *Phys Rev Lett* 2007;98(25):254503.
- Ba Y, et al. Color-gradient lattice Boltzmann model for simulating droplet motion with contact-angle hysteresis. *Phys Rev E Stat Nonlin Soft Matter Phys* 2013;88(4):043306.
- Rawool AS, Mitra SK, Kandlikar SG. Numerical simulation of flow through microchannels with designed roughness. *Microfluid Nanofluidics* 2005;2(3):215.
- Yang S, et al. Permeability model for fractal porous media with rough surfaces. *Microfluid Nanofluidics* 2014;18(5–6):1085.
- Oh JM, et al. Capillarity-driven dynamics of water–alcohol mixtures in nanofluidic channels. *Microfluid Nanofluidics* 2009;9(1):123.
- Wang M, Kang Q. Electrokinetic transport in microchannels with random roughness. *Anal Chem* 2009;81(8):2953.
- Wang M, Wang J, Chen S. Roughness and cavitations effects on electro-osmotic flows in rough microchannels using the lattice Poisson–Boltzmann methods. *J Comput Phys* 2007;226(1):836.
- Wenzel RN. Surface roughness and contact angle. *J Phys Chem* 1949;53(9):1466.
- Cassie ABD, Baxter S. Wettability of porous surfaces. *Trans Faraday Soc* 1944;40:546.
- Yang F-C, Chen X-P, Yue P. Surface roughness effects on contact line motion with small capillary number. *Phys Fluids* 2018;30(1):012106.
- Wolansky G, Marmur A. Apparent contact angles on rough surfaces: the Wenzel equation revisited. *Colloids Surf A Physicochem Eng Asp* 1999;156(1–3):381.
- Shardt N, Elliott JAW. Gibbsian thermodynamics of cassie-baxter wetting (Were Cassie and Baxter Wrong? Revisited). *Langmuir* 2018;34(40):12191.
- Harting J, Kunert C, Hyväluoma J. Lattice Boltzmann simulations in microfluidics: probing the no-slip boundary condition in hydrophobic, rough, and surface nanobubble laden microchannels. *Microfluid Nanofluidics* 2009;8(1):10.
- Dey P, Saha SK, Chakraborty S. Confluence of channel dimensions and groove width dictates slippery hydrodynamics in grooved hydrophobic confinements. *Microfluid Nanofluidics* 2020;24:23.
- Wang J, et al. Surface structure determines dynamic wetting. *Sci Rep* 2015;5(1):8474.
- Carlson A, Bellani G, Amberg G. Universality in dynamic wetting dominated by contact-line friction. *Phys Rev E Stat Nonlin Soft Matter Phys* 2012;85(4 Pt 2):045302.
- Mohammad Karim A, Rothstein JP, Kavehpour HP. Experimental study of dynamic contact angles on rough hydrophobic surfaces. *J Colloid Interface Sci* 2018;513:658.
- Huang JJ, et al. Numerical study of 2D multiphase flows over grooved surface by lattice Boltzmann method. *Int J Mod Phys C* 2007;18(04):492.
- Zhang L, et al. The effect of surface roughness on immiscible displacement using pore scale simulation. *Transp Porous Media* 2021;140(3):713.
- Quetzeri-Santiago MA, Castrejon-Pita AA, Castrejon-Pita JR. The effect of surface roughness on the contact line and splashing dynamics of impacting droplets. *Sci Rep* 2019;9(1):15030.
- Sari A, et al. Impact of surface roughness on wettability of oil-brine-calcite system at sub-pore scale. *J Mol Liq* 2020;299:112107.
- NVIDIA. **CUDA C programming guide. 2022.**
- Lishchuk SV, Care CM, Halliday I. Lattice Boltzmann algorithm for surface tension with greatly reduced microcurrents. *Phys Rev E Stat Nonlin Soft Matter Phys* 2003;67(3 Pt 2):036701.
- Halliday I, Hollis AP, Care CM. Lattice Boltzmann algorithm for continuum multicomponent flow. *Phys Rev E Stat Nonlin Soft Matter Phys* 2007;76(2 Pt 2):026708.
- Brackbill JU, Kothe DB, Zemach C. A continuum method for modeling surface tension. *J Comput Phys* 1992;100(2):335.
- Latva-Kokko M, Rothman DH. Diffusion properties of gradient-based lattice Boltzmann models of immiscible fluids. *Phys Rev E Stat Nonlin Soft Matter Phys* 2005;71(5 Pt 2):056702.
- Leclaire S, et al. Generalized three-dimensional lattice Boltzmann color-gradient method for immiscible two-phase pore-scale imbibition and drainage in porous media. *Phys Rev E* 2017;95(3–1):033306.
- Liu H, et al. Multiphase lattice Boltzmann simulations for porous media applications. *Comput Geosci* 2015;20(4):777.
- Xu Z, Liu H, Valocchi AJ. Lattice Boltzmann simulation of immiscible two-phase flow with capillary valve effect in porous media. *Water Resour Res* 2017;53(5):3770.
- Qian Y-H, d’Humières D, Lallemand P. Lattice BGK models for Navier-Stokes equation. *EPL (Europhysics Letters)* 1992;17(6):479.
- Guo Z, Zheng C, Shi B. Discrete lattice effects on the forcing term in the lattice Boltzmann method. *Phys Rev E Stat Nonlin Soft Matter Phys* 2002;65(4 Pt 2B):046308.
- Huang H, Huang J-J, Lu X-Y. Study of immiscible displacements in porous media using a color-gradient-based multiphase lattice Boltzmann method. *Comput Fluids* 2014;93:164.

- [60] Chen Y, et al. Inertial effects during the process of supercritical CO₂ displacing brine in a sandstone: lattice Boltzmann simulations based on the continuum-surface-force and geometrical wetting models. *Water Resour Res* 2019;55(12): 11144.
- [61] D'Humieres D, et al. Multiple-relaxation-time lattice Boltzmann models in three dimensions. *Philos Trans A Math Phys Eng Sci* 2002;360(1792):437.
- [62] Lallemand P, Luo LS. Theory of the lattice boltzmann method: dispersion, dissipation, isotropy, galilean invariance, and stability. *Phys Rev E Stat Phys Plasmas Fluids Relat Interdiscip Topics* 2000;61(6 Pt A):6546.
- [63] Guo Z, Shu C. *Lattice Boltzmann method and its application in engineering*, Vol. 3. World Scientific; 2013.
- [64] Leclaire S, Reggio M, Trépanier J-Y. Isotropic color gradient for simulating very high-density ratios with a two-phase flow lattice Boltzmann model. *Comput Fluids* 2011;48(1):98.
- [65] Akai T, Bijeljic B, Blunt MJ. Wetting boundary condition for the color-gradient lattice Boltzmann method: validation with analytical and experimental data. *Adv Water Resour* 2018;116:56.
- [66] Leclaire S, et al. Modeling of static contact angles with curved boundaries using a multiphase lattice Boltzmann method with variable density and viscosity ratios. *Int J Numer Methods Fluids* 2016;82(8):451.
- [67] Latva-Kokko M, Rothman DH. Static contact angle in lattice Boltzmann models of immiscible fluids. *Phys Rev E Stat Nonlin Soft Matter Phys* 2005;72(4 Pt 2): 046701.
- [68] Yu Y, et al. Color-gradient lattice Boltzmann modeling of immiscible two-phase flows on partially wetting surfaces. *Proc Inst Mech Eng Part C J Mech Eng Sci* 2017; 232(3):416.
- [69] Coope ID. Circle fitting by linear and nonlinear least squares. *J Optim Theory Appl* 1993;76(2):381.
- [70] Lafarge T, et al. Improved color-gradient method for lattice Boltzmann modeling of two-phase flows. *Phys Fluids* 2021;33(8):082110.
- [71] Huang JJ, Shu C, Chew YT. Lattice Boltzmann study of droplet motion inside a grooved channel. *Phys Fluids* 2009;21(2):022103.
- [72] Morrow NR. Capillary pressure correlations for uniformly wetted porous media. *J Can Pet Technol* 1976;15(04):49.